Environ. Sci.: Nano, 2021,8, 122-130

ARTICLE

Enhanced capacitive deionization of saline water using N-doped rod-like porous carbon derived from dual-ligand metal-organic frameworks

Received 00th January 20xx,
Accepted 00th January 20xx

DOI: 10.1039/x0xx00000x

Jing Zhang,[a‡] Tingting Yan,[a‡] Jianhui Fang,[a*] Junjie Shen,[b] Liyi Shi[a*] and Dengsong Zhang[a*]

Capacitive deionization (CDI) is a forward-looking technology that removes ions from brine due to its low energy consumption, low cost and prevention of secondary pollution. Removal capacity is still an issue for the CDI technology. It is quite urgent to design high performance CDI electrode material with reasonable porous structure, excellent conductivity and hydrophilic surface. Herein, we originally designed nitrogen-doped rod-like porous carbon derived from dual-ligand metal-organic frameworks (MOFs), in which two ligands, namely 1, 4-benzenedicarbocylic acid and triethylenediamine, to coordinate with zinc (Zn), respectively. The 1, 4-benzenedicarbocylic acid can be used as a pore-forming agent to increase the specific surface area of carbon material, and the triethylenediamine is used as nitrogen doping source to increase the hydrophilicity and conductivity of carbon material. By adjusting the ratio of two ligands, the optimal specific surface area and nitrogen doping for carbon material is obtained, thereby achieving the highest removal capacity for capacitive deionization of brine. The obtained carbon materials possess a hierarchical porous structure with moderate nitrogen doping. The large specific surface area of the electrode materials delivers many adsorption sites for adsorption of salt ions. The hierarchically porous structure provides a rapid transport channel of salt ions, and high-level N doping enhances conductivity and hydrophilicity for carbon materials to some extent. More importantly, the salt removal capacity of the electrodes is as high as 24.17 mg g^{-1} at 1.2 V in 500 mg L^{-1} NaCl aqueous solution. Hence, the moderate nitrogen doping porous carbon materials derived from dual-ligand MOFs is potential electrode material for CDI application. Such results open up a new method for preparation high performance electrodes to remove ions from saline water.

1. Introduction

The water scarcity is one of the biggest global problems facing the world in the 21st century. Population growth, industrial development and climate change further deteriorate the water crisis.[1] Removal of ions from brine or brackish water is an effective way to obtain fresh water. Capacitive deionization (CDI) is a potential technology for purifying water that uses electrostatic force to adsorb ions onto the porous structure of the charged electrodes.[2-5] Unlike conventional desalination methods, CDI, which removes ions from saline water, is faster and more easily.[6,7] High removal capacity and easy mass transfer of ion within electrode materials are crucial requirements for CDI.[8] The key of CDI technology is the design and fabrication of high performance electrodes, which have been evidenced previously.[9-14]

So far, a large amount of carbon materials such as activated carbons,[15] carbon aerogels,[16] graphene,[17-19] carbon nanotubes,[20] carbon-based composites,[21,22] mesoporous carbons,[23,24] hierarchically porous carbons[25-29], agricultural by-product derived porous carbon etc.[30] have been used as CDI electrode materials. However, due to the low specific surface area and poor conductivity of electrode materials, the wide application of CDI is limited. Removal capacity is still an issue for the CDI technology. Therefore, developing high performance CDI electrodes has attracted a great attention to promote the application of CDI technology for removal of ions from saline water.

Metal-organic frameworks (MOFs) are crystalline compounds formed by coordination and self-assembly of metal ions with organic ligands. Because of their large specific surface areas, adjustable pores, and unique architecture, MOFs have received extensive attention from researchers.[31-33] Recently, pyrolysis of MOFs has become a new strategy for preparation of porous carbon materials.[34-43] Due to high specific surface area and porous structure, carbon materials derived from MOFs are emerging as promising alternatives for CDI electrode materials.[44-48] Several MOFs-derived porous carbon have been designed and synthesized as CDI electrode in view of their

[a] Department of Chemistry, Research Center of Nano Science and Technology, Shanghai University, Shanghai 200444, PR China. E-mail: dszhang@shu.edu.cn (D. Zhang); jhfang@shu.edu.cn (J. Fang); shiliyi@shu.edu.cn (L. Shi).
[b] Department of Chemical Engineering, University of Bath, Bath BA2 7AY, UK.
† Electronic Supplementary Information (ESI) available. See
DOI: 10.1039/x0xx00000x
‡ These authors contributed equally to this work.

regular porous structures and open channels that are suitable for ion adsorption.[46-51] Liu et al. designated MOF-5-derived porous carbon and attained the salt removal capacity of 9.39 mg g^{-1}.[44] Pan et al. reported zeolitic imidazolate framework-8 (ZIF-8) derived porous carbon at different pyrolysis temperatures and after ZIF-8 was treated at 1200 °C, the porous carbon achieved the highest SAC of 13.86 mg g^{-1}.[45] Our group modified ZIF-8 by adding cetyltrimethylammonium bromide as in-situ pore expander, the CDI electrodes obtained by the pyrolysis of modified ZIF-8 showed an excellent SAC of 15.81 mg g^{-1}.[46] Our group also obtained the porous carbon by the pyrolysis of Al-based metal organic gels displayed a high SAC of 21.52 mg g^{-1} at 1.2 V in 500 mg L^{-1} NaCl solution.[49] The above descriptions indicate that MOFs-derived porous carbon materials are believed to be favored for high performance CDI applications.

Previous studies also indicated that doping nitrogen (N) into MOFs can effectively improve the hydrophilicity and conductivity of porous carbon electrodes.[47,48,52,53] Defects caused by N doping into carbon materials can increase the reactivity and electrical conductivity of carbon materials.[54-56] The N atom can provide free electrons with high electron affinity, thus increasing the positive charge density of adjacent carbon atoms and improving the conductivity of materials.[57] Some hydrophilic oxygen-containing functional groups will be introduced to improve the hydrophilicity of the materials.[48] N-doped carbon materials are beneficial for improving the electrosorption performance compared to non-atom doping. Literature indicates that for carbon materials, excellent specific surface area and heteroatom doping are important factors influencing CDI performance.[50, 58, 59] Controllable regulation of heteroatom doping and high specific surface area in MOFs has been achieved by regulating different ligands and metals. However, most of the MOFs materials reported in the literature are directly carbonized, or combined with other pore-forming agents and heteroatoms doping sources to achieve controllable regulation of MOFs-derived carbon materials.[46, 50, 51] Therefore, it is very meaningful to control the specific surface area and heteroatom doping of carbon materials by modulating the ligands of MOF and explore their effects on the CDI performance.

In this work, we investigate the effect of specific surface area and N-doping on the SAC of the carbon materials. For this, the traditional mono-ligand MOFs need to be compounded with other substances such as pore-forming agent, and extra N source. We controlled the ratio of two ligands, namely 1, 4-benzenedicarbocylic acid and triethylenediamine to coordinate with zinc (Zn), in order to achieve the controllable adjustment of morphology and composition of the MOFs material. The obtained moderate N-doped dual-ligand MOF-derived porous carbon material demonstrated a much improved SAC.

2. Materials and methods

2.1 Materials

Zinc nitrate hexahydrate ($Zn(NO_3)_2•6H_2O$) (99%) and Triethylenediamine (ted, 98%) were provided by Aladdin. 1, 4-benzenedicarbocylic acid (bdc, 99%) and N, N-Dimethylformamide (DMF) were provided by Sinopharm Chemical Reagent Co. Ltd. in China. All chemicals were directly used without further purification. Deionized water was used in all experiments.

2.2 Synthesis of the porous carbon materials

$Zn(NO_3)_2•6H_2O$ (0.455 g) and moderate ted (0.514 g) were stirred for 5 minutes in 15 mL DMF at room temperature, and bdc (0.761 g) was dissolved in 20 mL of DMF by heating at 60 °C. The two solutions were mixed in the 100 mL round bottom flask, then put it in the oil bath of 150 °C, and the vapors of liquid got condensed and refluxed. The reaction mixture reacted for 2 h with stirring, and was then placed in an oven for 20 h at 150 °C in order to slow evaporation of DMF from the mixture. After cooling the material to room temperature, washed 3-4 times with hot DMF (20-30 mL each time), followed by placing in the oven at 150 °C for 20 h, and in the vacuum oven at room temperature for 5 h. The obtained powder was dual-ligand MOF. The resultant powder was firstly heated to 200 °C and then to 900 °C for 2 h with a heating rate of 2 °C/min under nitrogen atmosphere and finally cooled to room temperature. Then, the resultant materials were etched thoroughly in a 2M HCl solution for 24 hours to remove residual Zn species. The moderate N-doped rod-like porous carbon derived from dual-ligand MOF (denoted as MNPC) was thus obtained.

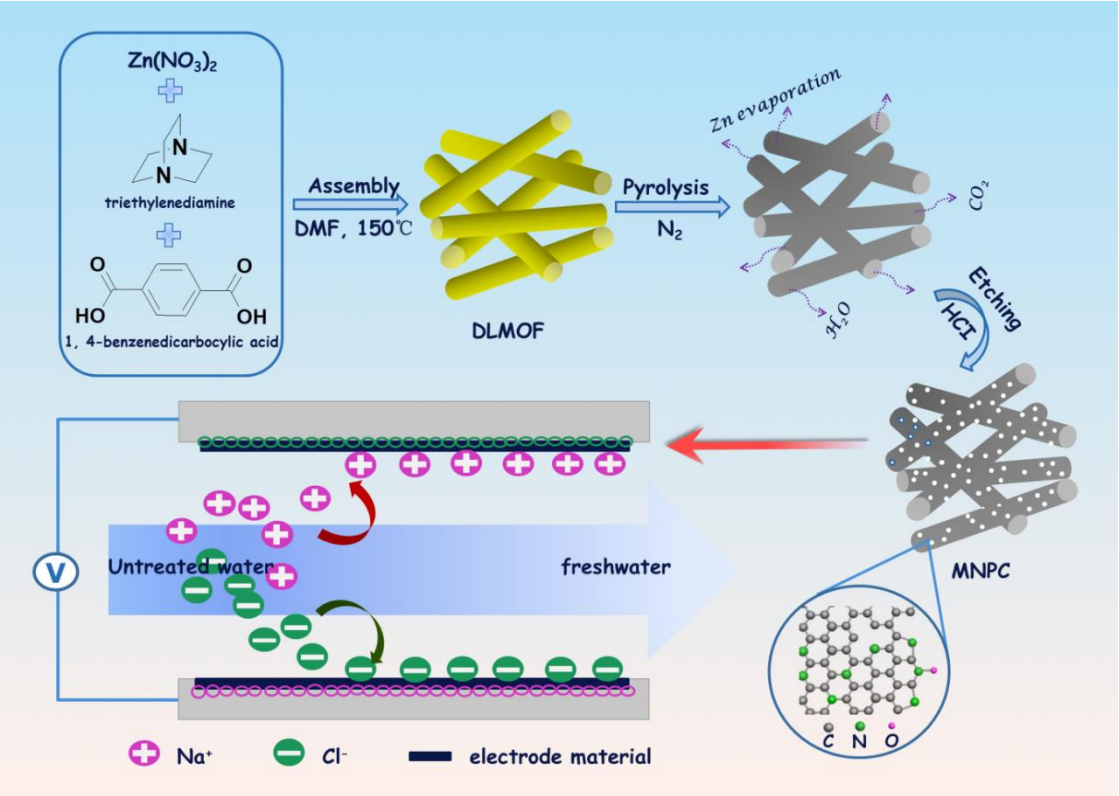

Fig. 1 Schematic illustration of N-doped rod-like porous carbon derived from dual-ligand MOF (MNPC) for CDI application.

For comparison, the amount of ted was changed to 0, 0.257 g and 1.028 g, respectively, and the comparative samples of porous carbon derived from mono-ligand MOF (denoted as PC), slight, and excessive N-doped rod-like porous carbon derived from dual-ligand MOF (denoted as SNPC and ENPC) were obtained by using the similar method. The overall synthesis route for the fabrication of MNPC and its CDI application is depicted in Fig. 1.

2.3 Materials characterization

The samples were characterized by using a transmission electron microscope (TEM, JEOL JEM-200CX) and a field emission scanning electron microscope (FESEM, JEOL JEM-700F). High resolution transmission electron microscopy (HRTEM) images were recorded using a JEOL JEM-2010F instrument. X-ray diffraction (XRD) pattern were obtained using a Rigaku D/MAX-RB X-ray diffractometer (Cu Ka, 40 kV, 20 mA). The nitrogen adsorption–desorption isotherms were measured on Autosorb-IQ2 (Quantachrome Corporation). The specific surface area was obtained by the Brunauer-Emmett-Teller (BET) method. The pore size distribution was analyzed by the slit/cylinder pores QSDFT adsorption model. The micropore surface area (S_{micro}) and micropore volume (V_{micro}) were obtained from t-plot analysis. The Raman spectroscopy was performed to study the structure of the carbon materials. X-ray photoelectron spectroscopy (XPS) was conducted on a PerkinElmer PHI 5000C ESCA system equipped with a dual X-ray source, using a 45 Mg Ka (1253.6 eV) anode and a hemispherical energy analyser. The hydrophilicity of the electrode materials was tested by a drop shape analysis system (Kruss, DSA100).

2.4 Electrochemical characterization

Cyclic voltammetry (CV), galvanostatic charge-discharge (GCD) and electrochemical impedance spectroscopy (EIS) of electrode materials were tested using electrochemical workstations CHI 660D (Shanghai Chenhua, China). The PC, SNPC, MNPC and ENPC electrodes were used as working electrodes (2 cm × 2 cm), respectively. The counter electrode was graphite electrode, and the reference electrode was saturated calomel electrode. For all working electrodes, the mass was 0.005 g, and the concentration of NaCl solution was 0.5 M. CV curves were measured at different scan rates, such as 1, 5, 10, 20, 50 and 100 mV s^{-1} in 0.5 M and 500 mg L^{-1} NaCl solution. The applied voltage range was from -0.5 V to 0.5 V. When the concentration of NaCl solution is higher, the salt ions accumulate and adsorb on the electrode surface better, resulting in higher electron conductivity and more ion content in the electric double-layer region.[60] The specific capacitance of PC, SNPC, MNPC and ENPC was estimated from CV based on the equation (1),

$$C_m = \frac{\int I\,dV}{2v\Delta V m} \quad (1)$$

Where, C_m (F g^{-1}) representatives specific capacitance, I (A), v (mV s^{-1}), ΔV (V) and m (g) representative current density, scan rate, voltage change and mass of electrodes, respectively.

2.5 CDI performance

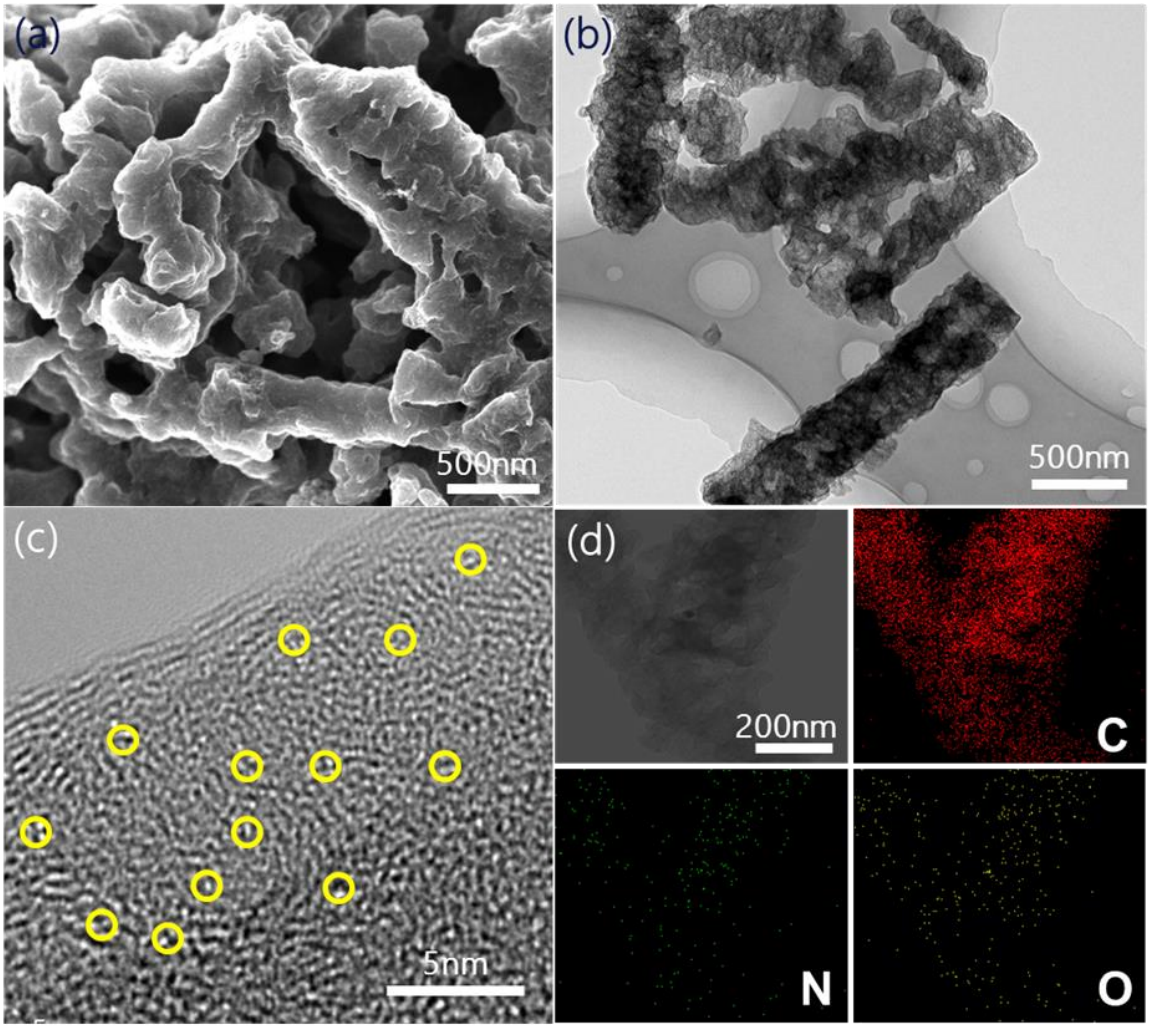

Fig. 2 Microstructure characterization of MNPC. (a) SEM image, (b) TEM image, (c) HRTEM image and (d) EDS mapping of MNPC.

The CDI electrodes are composed of 80 wt% of PC, or SNPC, or MNPC, or ENPC, 10 wt% of PTFE (Poly tetra fluoroethylene) and 10 wt% of Super P (a conductive additive). These components were uniformly mixed in ethanol and then compacted on graphite paper to form a film. The graphite paper coated with the material was then dried in an oven at 120 °C overnight to obtain a CDI electrode. Finally, the electrodes were assembled into a self-made desalination apparatus to detect salt electrosorption performance. For each pair of electrode, the total mass of sample was 0.12 g, the coated area was 60 mm × 62 mm, and the thickness of the coated film was 0.1 mm. The ambient temperature and the total volume of the NaCl solution in the desalination experiment were maintained at 298 K and 50 mL, respectively. The original concentration of NaCl aqueous solution used in the desalination system is 50, 100, 300, 500 mg L^{-1}, respectively. The applied voltage at both ends of the electrodes is 0.8, 1.0, 1.2 V, respectively. The SAC of PC, SNPC, MNPC and ENPC electrodes were calculated using the following formula (2):

$$SAC = \frac{(C_0 - C)V}{m} \quad (2)$$

The salt removal percentage can be calculated as follows:

$$\%\Delta salt = \frac{(C_0 - C)\times 100\%}{C} \quad (3)$$

Where, C_0, C and V represent the original concentration (mg L^{-1}), equilibrium concentration (mg L^{-1}) of NaCl solution and total volume (L) of NaCl solution, respectively, m represents total mass of active materials (g).

The salt adsorption rate, SAR, was obtained using the equation:

$$SAR = \frac{SAC}{t} \quad (4)$$

Where, t is electrosorption time (s).

The charge efficiency, Λ, is estimated according to the equation:

$$\Lambda = \frac{\Gamma \times F}{\sum} \quad (5)$$

Where, Γ (mol g^{-1}) and F (96485 C mol^{-1}) represents deionization capacity and the Faraday constant, respectively. ∑ is obtained using integrating current (charge, C g^{-1}).

3. Results and discussion

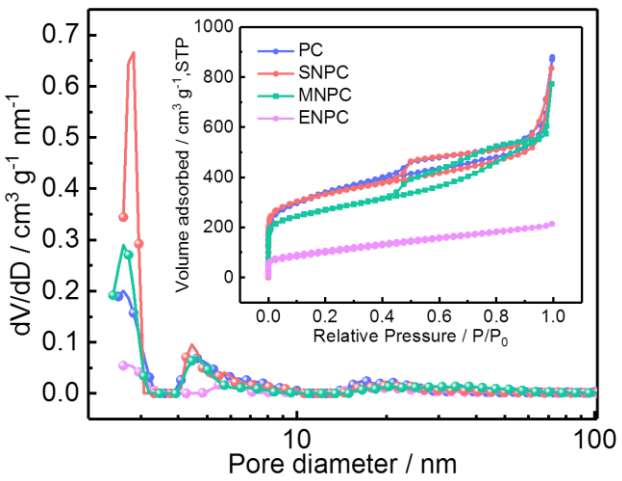

Fig. 3 The pore size distribution profiles of all samples. The insets show the nitrogen adsorption-desorption isotherms of all samples.

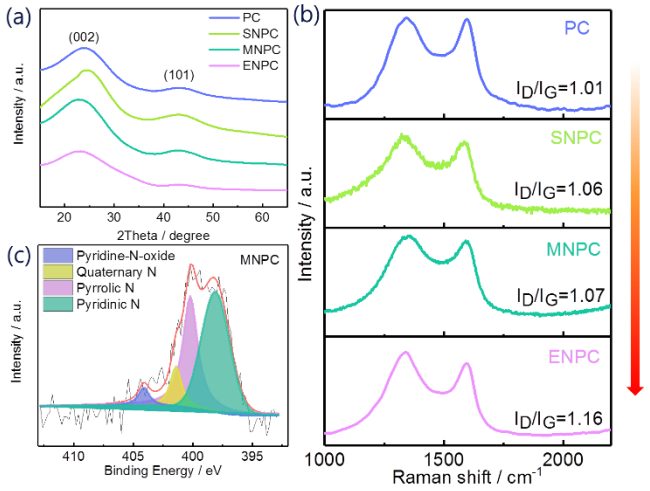

Fig. 4 (a) XRD patterns and (b) Raman spectra of the PC, SNPC, MNPC and ENPC. (c) High-resolution N1s spectrum of the MNPC samples.

3.1 Characteristics

In DMF solvent, 1, 4-benzenedicarbocylic acid (bdc) and moderate triethylenediamine (ted) could simultaneously coordinate with Zn to form the dual-ligand MOF. The H_2O and CO_2 gas were released due to decomposition of bdc during calcination, and Zn particles evaporated under high temperature (907 °C) causing a lot of porous structures and high specific surface area. The pyrolysis of ted ligand doped the N element into the carbon material. After that, impurities were removed by hydrochloric acid etching to obtain the moderate N-doped rod-like porous carbon material (MNPC). As shown in Fig. 2, the morphology of MNPC is a rod-like structure with a rough surface. While, the porous carbon (PC) derived from the mono-ligand MOF was bulk material (Fig. S1a and d†). The slight N-doped rod-like porous carbon (SNPC) with a rough surface was obtained after pyrolysis of dual-ligand MOF (Fig. S1b and e†). With increase of ted ligand, the obtained dual-ligand MOF derived excessive N-doped porous carbon (ENPC) was rod-like structure with smooth surface and less pores (Fig. S1c and f†). As it shown at Fig. 2a and b, MNPC has a rod-like structure composed of coarse particles with many holes, which helps to increase the specific surface area of material. There are some mesopores and macropores between rod and rod, which can facilitate the transfer and diffusion of salt ions in the material. The presence of abundant micropores can be seen in the portions marked by the yellow circles in Fig. 2c, which promote the adsorption of salt ions in the material. It can also be seen that MNPC is an amorphous structure. In addition, it can be seen from the elemental mapping analysis in Fig. 2d that N and O elements in MNPC are homogenously distributed throughout the rod-like porous carbon material. The presence of O can be attributed to H_2O, O_2 and CO_2 in the atmosphere adsorbed on the rod-like porous carbon material. This kind of porous framework is highly essential for CDI electrodes, because the porous channels are helpful for rapid transport and adsorption of salt ions within the MNPC electrode matrix.

In order to explore the physical adsorption characteristics of PC, SNPC, MNPC and ENPC, N_2 adsorption/desorption experiments were performed. As shown in the inset of Fig. 3, most of curves show type-IV isotherms. When $p/p_0<0.1$, the amount of N_2 adsorption has a sharp increase, indicating the adsorption characteristics of the micropores. At a relatively high pressure starting at about 0.45, a hysteresis loop appears in the curve, indicating the presence of mesopores in the material skeleton.[36,39] The pore size distribution data calculated by the QSDFT method in Fig. 3 has been further analyzed. The PC, SNPC and MNPC all exhibit mesoporous distribution peaks at 2.6, 4.6, and 17 nm. The specific surface area and pore volume data of all samples are shown in Table S1†. The results show that the specific surface area and pore volume of MOFs derived carbon materials decrease with addition of ted ligand, which corresponds to the morphology analysis results. It has been stated that such MNPC material may not only support the formation of N-active sites but also could be carefully controlled their suitable specific surface area according to need in CDI.

The graphite properties of carbon materials were characterized by XRD and Raman spectroscopy. The XRD patterns of PC, SNPC, MNPC and ENPC are shown in Fig. 4a. At 23° and 43°, there are two diffraction peaks, which represent (002) and (101) lattice planes of carbon, respectively.[36] From the low intensity and broad peaks of XRD patterns, it is known that these MOFs-derived carbon materials are non-graphitize and amorphous nature, which is consistent with TEM data. The successful preparation of pure carbon materials is confirmed by the absence of other diffraction peaks, which indicate that Zn species are totally removed during acid etching. The structure disorder of carbon-based materials can be characterized by Raman spectroscopy. Both the D and G bands are Raman characteristic peaks of the C atom crystal: the G peak belongs to the E_{2g} vibration mode due to the extension of the bond of all sp^2 atoms in the chain and the ring; and the D peak is attributed to the breathing pattern of sp^2 atom in the ring, which corresponds to defects and disorder within the carbon matrix.[61,62] The Raman spectra of PC, SNPC, MNPC and ENPC are shown in Fig. 4b. The D and G bands appear around 1323 cm^{-1} and 1590 cm^{-1}. The I_D/I_G of PC, SNPC, MNPC and

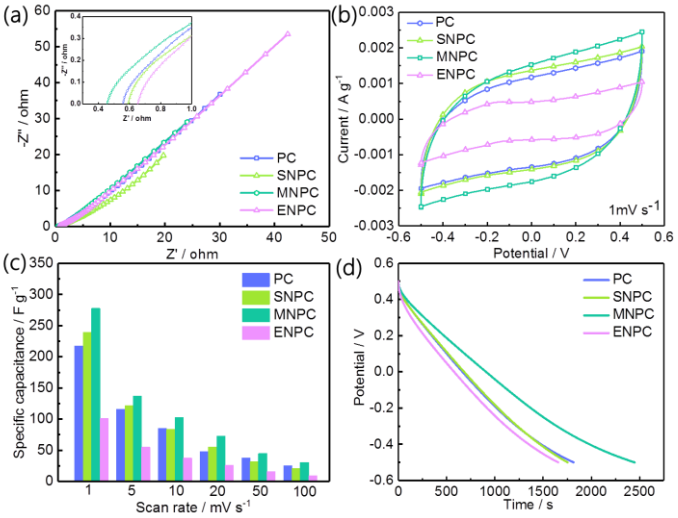

Fig. 5 Electrochemical properties of the PC, SNPC, MNPC and ENPC electrodes. (a) the Nyquist plots, the inset is the magnified area, (b) cyclic voltammograms at a scan rate of 1 mV s^{-1}, (c) specific capacitance at different scan rates and (d) galvanostatic discharge at a current density of 200 mA g^{-1}. All the curves were obtained in a 0.5 M NaCl solution.

ENPC is 1.01, 1.06, 1.07 and 1.16, respectively, suggesting that with the increases of ted ligand, the degree of disorder and defect increases.[63] The results show that the doping of N-atoms due to ted ligand, more defect structure is introduced into the carbon material. In summary, the XRD and Raman results confirm that MNPC is amorphous in nature and more defective sites are produced.

The elemental composition and bonding state of each element in the carbon materials were further analyzed by XPS spectroscopy. The XPS survey of SNPC, MNPC and ENPC is shown in Fig. S2†. Moreover, the content of N in SNPC, MNPC and ENPC is 1.84%, 2.60% and 4.54%, respectively. As shown in Fig. 4c, Fig. S3a and Fig. S3b, high-resolution N_{1s} spectra of MNPC, SNPC and ENPC is fitted into four forms such as pyridinic N-oxide, graphitic nitrogen, pyrrolic nitrogen and pyridinic nitrogen, which are located at 404.1 eV, 401.4 eV, 400.2 eV and 398.1 eV, respectively. For the MNPC, the relative contents of various doping forms of N atom are 36.2% pyrrolic-N, 49.7% pyridinic-N, 9.7% graphitic-N, and 4.4% pyridinic-N-oxide, respectively. Pyridinic-N and graphitic-N are sp^2 hybridized, while pyrrolic-N is sp^3 hybridized. Pyridinic-N binds to two C atoms at the edge or defect of carbon network and contributes one p electron to the p system. Pyrrolic-N means that the N atom contributes two p electrons to the p system. Pyridinic-N and pyrrolic-N provide lone electron pairs and act as electron donors. Because pyridinic-N has a single lone pair of electrons, it is considered an active catalytic center by various research groups.[64] At the same time, defects are created to provide channels and active sites, thereby increasing the pseudocapacitance. And graphitic-N refers to the replacement of the C atom by N atom in the hexagonal ring. Graphitic-N promotes electron transfer within the carbon matrix, thereby improving the conductivity of carbon.[65] N-containing group, pyridinic-N-oxide provides high hydrophilicity of the material.[66] The increase of N doping content will lead to an increase of defects in the graphite structure, and moderate N doping can effectively improve the conductivity and hydrophilicity of carbon materials. When the defects reach a certain level, it will hinder the migration of electrons in the material. The non-conductive a-CN_x phase is formed in the carbon material, thereby reducing the electrical conductivity.[67, 68] Compared with PC and SNPC, MNPC has a higher level of N doping. Compared to ENPC, MNPC has a higher specific surface area, so comprehensively considering, MNPC has a moderate N doping and the suitable specific surface area, revealing the best electrochemical property. Therefore, these excellent properties suggest good CDI performance of MNPC.

In order to check hydrophilicity of electrode materials, we conducted dynamic contact angle experiment. Fig. S4† shows the contact angle of PC, SNPC, MNPC and ENPC electrodes, respectively. When the water droplet just touches the surface of material, the contact angle of MNPC (95.19°) is lower than those of PC (98.90°), SNPC (98.25°) and ENPC (115.49°). In comparison, the contact angle of MNPC electrode decrease more rapidly with time. After 120 s, final contact angles of PC, SNPC, MNPC and ENPC decrease to 71.90°, 76.77°, 60.67° and 107.27°, respectively. Clearly, the hydrophilicity of the MNPC electrode is stronger than other samples. The improvement in wettability is mainly due to the hierarchical porous structure and suitable N-atom doping of MNPC. The enhanced wettability of MNPC allows the electrode to have a good compatibility with aqueous solutions, which helps salt ions to more easily enter into the pore channels of carbon materials, thereby improving CDI performance.

3.2 Electrochemical performance

To demonstrate the CDI capability of electrode materials, we tested the electrochemical performance of PC, SNPC, MNPC and ENPC. The electrical resistance generated during electrochemical process including the contact resistance of electrolytic ions with pores, the charge transfer resistance and the diffusion resistance can be described by EIS. As shown in Fig. 5a, a small semicircle appears in high frequency region, and its intercept on the real axis related to equivalent series resistance (ESR).[69] It can be seen from the enlarged view in Fig. 5a that the ESR value of MNPC electrode is smaller than that of PC, SNPC and ENPC electrodes. MNPC exhibits more vertical line in the low frequency region compared to other samples, indicating good ion diffusion inside MNPC material.[70] The smaller ESR and faster ion diffusion of MNPC electrode facilitate excellent capacitive performance of material.

The CV experiments were also performed to characterize the capacitive behavior of the electrode materials. As the Fig. 5b shows, CV curves of PC, SNPC, MNPC and ENPC exhibit all near rectangular in shape, and no significant redox peaks appear, revealing that adsorption process is an ideal capacitive behavior.[71] At the scan rate of 1mV s^{-1}, specific capacitance of PC, SNPC, MNPC and ENPC electrodes calculated by eqn (1) was 217.4, 239.5, 277.7 and 101.34 F g^{-1}, respectively (Fig. 5b). Clearly, compared with other materials, MNPC has higher specific capacitance, which is also higher than that of other reported literature under the same conditions, as shown in Table S2†, which corresponds to a higher SAC value. At different scan rates, such as 1, 5, 10, 20, 50 and 100 mV s^{-1}, CV curves of PC, SNPC, MNPC and ENPC show a nearly rectangular

shape, indicating good ion transport channels and electronic conductivity (Fig. S5†). As shown in Fig. 5c, at any scan rate, specific capacitance of MNPC is always higher than those of PC, SNPC and ENPC. This results shows that MNPC has better electric double layer capacitor (EDLC) performance than PC, SNPC and ENPC. The CV of PC, SNPC, MNPC and ENPC electrodes at low NaCl concentrations of 500 mg L^{-1} is also tested, as shown in Fig. S6†. The calculated the specific capacitances of PC, SNPC, MNPC and ENPC electrodes at the scan rate of 1 mV s^{-1} are 37.8, 56.1, 135.2 and 37.7 F g^{-1}, respectively, which indicating that MNPC has better electrochemical performance. The specific capacitances of MNPC electrodes are 135.2, 51.0, 33.3, 21.9, 8.8 and 5.5 F g^{-1} at the scan rate of 1 mV s^{-1}, 5 mV s^{-1}, 10 mV s^{-1}, 20 mV s^{-1}, 50 mV s^{-1} and 100 mV s^{-1}, respectively. The results are consistent well with that of these CV results at 0.5 M NaCl solution. The outstanding capacitive behavior is attributed to the enhanced conductivity and hydrophilicity of MNPC, which facilitates fast ion adsorption.

The electrochemical property of electrodes was further characterized using the GCD test. Fig. 5d shows discharge curves of PC, SNPC, MNPC and ENPC at the current density of 200 mA^{-1} with the potential range of -0.5~0.5 V in the NaCl solution. Compared with other samples, MNPC shows a longer discharge time, indicative of higher capacitance value, which is consistent well with the CV analysis results. When changing the current density, the GCD curves of MNPC are shown in Fig. S7†. All GCD curves exhibit linear and symmetrical triangles, exhibiting the exceptional EDLC behavior, good rate capability and excellent reversibility. Therefore, these distinctive features of MNPC electrode are thought to be helpful for CDI applications.

3.3 CDI performance

To explore CDI performance of electrodes, the salt adsorption capacity (SAC) of PC, SNPC, MNPC and ENPC electrodes were tested at 1.2 V, in the NaCl solution of 500 mg L^{-1}, at the flow rate of 50 mL min^{-1}. The SAC values of all electrodes change with deionization time as shown in Fig. 6a. As long as electric field was applied, conductivity of solution dropped sharply because sodium ions and chloride ions were rapidly adsorbed on the surface of electrodes with opposite charges, leading to a sharp increase in the SAC value. It is clear that most of the salt ions were adsorbed, the SAC increased slowly, indicating that the electrosorption equilibrium was gradually completed. The SAC value calculated by eqn (2) for MNPC electrodes reached to 24.17 mg g^{-1} at 120 min, which is higher than those of PC (18.54 mg g^{-1}), SNPC (20.21 mg g^{-1}) and ENPC (12.08 mg g^{-1}), respectively. Moreover, the MNPC electrodes exhibit a higher SAC value under the similar test conditions than any other carbon materials reported in the literatures (Table 1).

Table 1. Comparison of adsorption capacity of reported carbon materials.

Electrode materials	Applied voltage [V]	Initial NaCl concentration [mg L^{-1}]	Adsorption capacity [mg g^{-1}]	Ref.
N-doped porous carbon spheres	1.2	500	13.71	72
Porous carbon polyhedra	1.2	500	13.86	45
Nitrogen-doped carbon nanorods	1.2	500	17.62	73
Rod-like nitrogen-doped carbon hollow shells	1.2	250	13.38	74
Micro/mesoporous carbon sheets	1.2	500	17.38	75
Graphene bonded carbon nanofiber aerogels	1.2	500	15.7	76
3D Intercalated Graphene Sheet-Sphere Nanocomposite	1.2	500	22.09	18
3D graphene	1.2	500	14.7	77
N-doped porous hollow carbon spheres	1.4	500	12.95	78
Hollow ZIFs-derived nanoporous carbon	1.2	500	15.31	79
Sandwich-like nitrogen-doped graphene	1.2	500	14.5	17
MOF/polypyrrole hybrid	1.2	584	11.34	80
nitrogen-doped mesostructured carbons	1.2	584	20.63	58
MNPC	1.2	500	24.17	This work

In general, the CDI process of porous electrodes involves the following four parts: (I) ions diffuse in an aqueous solution; (II) ions transfer into pores channels of electrode; (III) electrosorption of ions in electric double layer of electrode; and (IV) ions transfer from electrode to brine.[81] The MNPC has a suitable specific surface area and pore size, which provides more adsorption sites for salt ions. During electrosorption process, micropores provide the adsorption sites of salt ions, and mesopores are more conducive to the transport of salt ions in materials. The suitable pore size distribution ensures the rapid adsorption of salt ions in the electrode. N-doping in MNPC also improves the wettability and conductivity of carbon materials, which is conducive to the electroadsorption of electrodes in aqueous solution.

The desalination performance of these samples was also tested in 50 mg L^{-1} NaCl solution. As the Fig. S8† shows, the salt removal percentage of PC, SNPC, MNPC and ENPC reached 63%, 75%, 83% and 53%, respectively. Therefore, the salt removal percentage of MNPC is higher than those of PC, SNPC and ENPC electrodes, and is comparable to the values reported in the literature under the same conditions, as shown in Table S3†, which reflects the better CDI performance of MNPC.

The salt adsorption rate (SAR) and SAC can be described by using Ragone curves. We have also studied several general parameters affecting desalination performance, such as different carbon materials, salt concentration and voltage, etc., to fully check CDI performance of electrodes. Fig. 6b shows the Ragone plots of SAR and SAC for PC, SNPC, MNPC and ENPC in the NaCl solution of 500 mg L^{-1} at 1.2V. It can be seen that Ragone curve of MNPC is in upper right, which indicates that MNPC has a higher SAR and SAC. The reason is that MNPC has the higher specific surface area, more suitable pore size distribution and moderate amount of nitrogen doping, so that salt ions can be quickly transported and adsorbed in the pore.

The applied voltage and the concentration of NaCl solution are also the important factors affecting the CDI performance of electrodes. Therefore, the SAR and SAC of MNPC at different applied voltages of 0.8, 1.0 and 1.2 V and different concentrations of NaCl solution such as 100, 300 and 500 mg L^{-1} were also investigated. Fig. 6c shows the variation of SAC values with time under different applied voltages for MNPC.

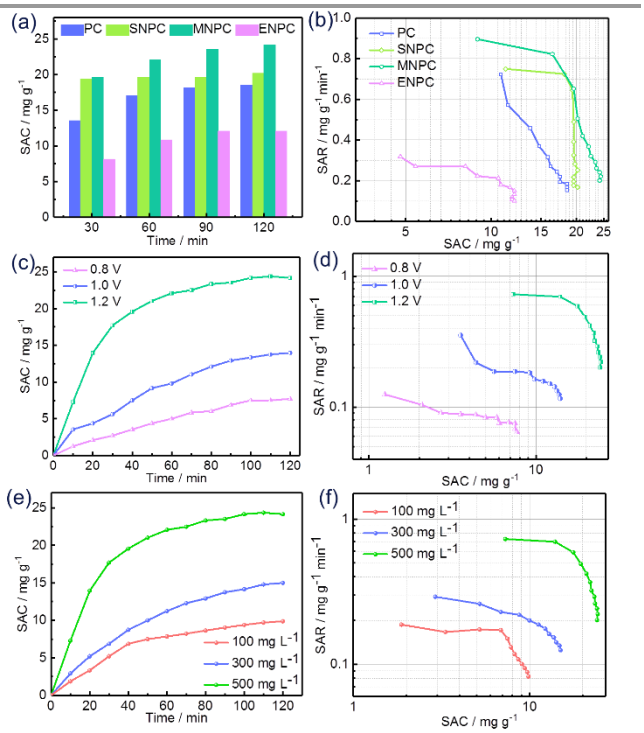

Fig. 6 (a) Plots of SAC vs. time, and (b) Ragone plots of various electrodes in 500 mg L^{-1} NaCl solution at 1.2 V. (c) Plots of SAC vs. time, and (d) Ragone plots of MNPC electrodes in 500 mg L^{-1} NaCl solution at different cell voltages. (e) Plot of SAC vs. time and (f) Ragone plots of the MNPC electrodes in different concentrations of NaCl solution at 1.2 V. The flow rate is 50 mL min^{-1}, same for all desalination experiments.

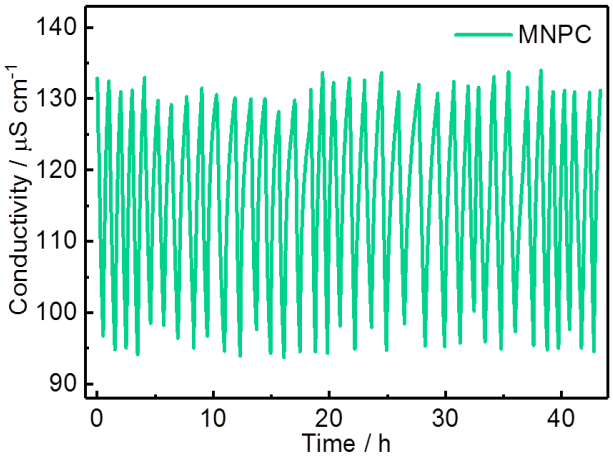

Fig. 7 Regeneration curve of the MNPC electrodes in a 100 mg L^{-1} NaCl solution at the charge voltage of 1.2 V and the discharge voltage of 0 V.

Initially, the SAC of MNPC increases rapidly with time, and then increases slowly until the electrosorption reaches equilibrium after 120 minutes. When applied voltage increases from 0.8 V to 1.2 V, the SAC of MNPC also increases from 7.71 to 24.71 mg g^{-1}. At a higher applied voltage, the MNPC electrode exhibits a higher SAC. This is because a higher voltage induces a stronger electrostatic interaction, thereby adsorbing a larger amount of salt ions from the solution. The Ragone plots of SAR versus SAC for MNPC at different applied voltages is shown in Fig. 6d. As can be seen from the graph, increasing the voltage shifts the curve toward the upper right, which indicates that the SAR and SAC increase as the applied voltage increases. The SAC of MNPC in different NaCl concentrations as the function of time is shown in Fig. 6e. When concentration of NaCl solution increases from 100 to 500 mg L^{-1}, the SAC value of MNPC increases from 9.88 to 24.17 mg g^{-1}. As the Fig. 6f shows, the Ragone curves display that at higher salt concentration, the curve moves to upper right, displaying the higher SAC and SAR. The increase in SAC is mainly attributed to the formation of a more compact electric double layer capacitor in higher concentration. The increase in SAR is due to the higher conductivity of the solution, and the rapid transfer of the ions from solution to electrodes.[82,83]

The electrode material used is carbon material obtained by annealing the MOF precursors in an inert atmosphere and then washed with acid, which has relatively stable physical and chemical property. The cyclic stability of electrodes is critical for CDI applications, so continuous adsorption-regeneration more than 35 cycles was performed on the MNPC electrodes in the NaCl solution of 100 mg L^{-1} at 1.2 V applied voltage to evaluate the stability. As shown in Fig. 7, at the beginning of the CDI process, the conductivity of the solution decreased because the electrolyte was attracted by the oppositely charged electrodes and stored in the electric double layer. When the adsorption process of electrolyte on the electrode was completed, a short-circuit voltage was applied to regenerate the MNPC electrodes. Therefore, due to desorption of the adsorbed salt ions, the conductivity of the solution increased again, and the concentration of the salt solution quickly returned to the original concentration. After 35 cycles,

the MNPC electrode remained stable without significant degradation in performance, indicating that the MNPC electrodes have good stability after continuous electrosorption-desorption cycles.

The charge utilization and energy loss during desalination can be measured by charge efficiency (Λ).[6,84] The charge efficiency for MNPC in different NaCl concentrations at 1.2 V applied voltage was showed in Fig. S9†. The Λ values in the 100~500 mg L^{-1} NaCl solution were calculated according to equation (5) to be 0.58, 0.73 and 0.82, respectively. It is obvious that the charge efficiency of MNPC electrodes decreases with the reducing of NaCl concentration, which is consistent well with the literatures.[18,73,85-87] The high charge efficiency of the MNPC electrodes indicates its low energy consumption during the CDI process.

Conclusions

In conclusion, we originally synthesized moderate N-doped rod-like porous carbon derived from dual-ligand MOF, which shows high specific surface area, appropriate pore size distribution, enhanced hydrophilic and electrical conductivity. Enhanced removal of ions from saline water by MNPC electrodes via capacitive deionization has been demonstrated. In CDI tests, the SAC of MNPC electrodes achieved the highest removal capacity of 24.17 mg g^{-1}. The high specific surface area, good porous structure and moderate N-doping of the carbon material enhance removal of ions from saline water. The moderate N-doped rod-like porous carbon derived from the dual-ligand MOF should be a potential CDI electrode material. This work provides a new idea for designing multi ligands with different functions (such as ligands containing different heteroatoms) to coordinate with different metals (Co, Ni, Fe, etc.) to achieve the regulation of properties of derived carbon materials. It also opens up new methods for design of high-performance electrode materials for capacitive deionization of saline water.

Conflicts of interest

There are no conflicts to declare.

Acknowledgements

This work was supported by the National Key R&D Program of China (2017YFB0102200), the National Natural Science Foundation of China (21906101) and the Science and Technology Commission of Shanghai Municipality (19DZ2293100; 18DZ2281400).

Notes and references

1. C. J. Vorosmarty, P. B. McIntyre, M. O. Gessner, D. Dudgeon, A. Prusevich, P. Green, S. Glidden, S. E. Bunn, C. A. Sullivan, C. R. Liermann and P. M. Davies, Global threats to human water security and river biodiversity, *Nature*, 2010, **467**, 555-561.
2. P. Liu, T. Yan, L. Shi, H. S. Park, X. Chen, Z. Zhao and D. Zhang, Graphene-based materials for capacitive deionization, *J. Mater. Chem. A*, 2017, **5**, 13907-13943.
3. Z.-H. Huang, Z. Yang, F. Kang and M. Inagaki, Carbon electrodes for capacitive deionization, *J. Mater. Chem. A*, 2017, **5**, 470-496.
4. C.-H. Hou and C.-Y. Huang, A comparative study of electrosorption selectivity of ions by activated carbon electrodes in capacitive deionization, *Desalination*, 2013, **314**, 124-129.
5. H. Li, L. Pan, T. Lu, Y. Zhan, C. Nie and Z. Sun, A comparative study on electrosorptive behavior of carbon nanotubes and graphene for capacitive deionization, *J. Electroanal. Chem.*, 2011, **653**, 40-44.
6. M. E. Suss, S. Porada, X. Sun, P. M. Biesheuvel, J. Yoon and V. Presser, Water desalination via capacitive deionization: what is it and what can we expect from it? *Energy Environ. Sci.*, 2015, **8**, 2296-2319.
7. W. Zhang and B. Jia, Toward anti-fouling capacitive deionization by using visible-light reduced TiO_2 graphene nanocomposites. *MRS Communications*, 2015, **5**, 613-617.
8. A. v. d. W. S. Porada，R. Zhao, V. Presser , P.M. Biesheuvel, Review on the science and technology of water desalination by capacitive deionization, *Prog. Mater. Sci.*, 2013, **58**, 1388 – 1442.
9. G. Wang, Q. Dong, T. Wu, F. Zhan, M. Zhou and J. Qiu, Ultrasound-assisted preparation of electrospun carbon fiber/graphene electrodes for capacitive deionization: Importance and unique role of electrical conductivity, *Carbon*, 2016, **103**, 311-317.
10. Q. Dong, G. Wang, B. Qian, C. Hu, Y. Wang and J. Qiu, Electrospun Composites Made of Reduced Graphene Oxide and Activated Carbon Nanofibers for Capacitive Deionization, *Electrochim. Acta*, 2014, **137,** 388-394.
11. S. Wang, G. Wang, T. Wu, C. Li, Y. Wang, X. Pan, F. Zhan, Y. Zhang, S. Wang and J. Qiu, Membrane-Free Hybrid Capacitive Deionization System Based on Redox Reaction for High-Efficiency NaCl Removal, *Environ. Sci. Technol.*, 2019, **53**, 6292-6301.
12. S. Wang, G. Wang, X. Che, S. Wang, C. Li, D. Li, Y. Zhang, Q. Dong and J. Qiu, Enhancing the capacitive deionization performance of $NaMnO_2$ by interface engineering and redox-reaction, *Environ. Sci.: Nano*, 2019, **6**, 2379-2388.
13. G. Wang, B. Qian, Q. Dong, J. Yang, Z. Zhao and J. Qiu, Highly mesoporous activated carbon electrode for capacitive deionization, *Sep. Purif. Technol.*, 2013, **103**, 216-221.
14. T. Wu, G. Wang, F. Zhan, Q. Dong, Q. Ren, J. Wang and J. Qiu, Surface-treated carbon electrodes with modified potential of zero charge for capacitive deionization, *Water Res.*, 2016, **93**, 30-37.
15. R. L. Zornitta, J. J. Lado, M. A. Anderson and L. A. M. Ruotolo, Effect of electrode properties and operational parameters on capacitive deionization using low-cost commercial carbons, *Sep. Purif. Technol.*, 2016, **158**, 39-52.
16. M. Haro, G. Rasines, C. Macias and C. O. Ania, Stability of a carbon gel electrode when used for the electro-assisted removal of ions from brackish water, *Carbon*, 2011, **49**, 3723-3730.

17. T. Yan, J. Liu, H. Lei, L. Shi, Z. An, H. S. Park and D. Zhang, Capacitive deionization of saline water using sandwich-like nitrogen-doped graphene composites via a self-assembling strategy, *Environ. Sci.: Nano*, 2018, **5**, 2722-2730.
18. Z. U. Khan, T. Yan, L. Shi and D. Zhang, Improved capacitive deionization by using 3D intercalated graphene sheet–sphere nanocomposite architectures, *Environ. Sci.: Nano,* 2018, **5**, 980-991.
19. H. Wang, P. Liu, T. Yan, J. Zhang, L. Shi and D. Zhang, Grafting sulfonic and amine functional groups on 3D graphene for improved capacitive deionization, *J. Mater. Chem. A,*, 2016, **4**, 5303–5313.
20. M. A. Tofighy and T. Mohammadi, Salty water desalination using carbon nanotube sheets, *Desalination*, 2010, **258**, 182-186.
21. D. Zhang, T. Yan, L. Shi, Z. Peng, X. Wen and J. Zhang, Enhanced capacitive deionization performance of graphene/carbon nanotube composites, *J. Mater. Chem.*, 2012, **22**, 14696.
22. Z. Peng, D. Zhang, L. Shi and T. Yan, High performance ordered mesoporous carbon/carbon nanotube composite electrodes for capacitive deionization, *J. Mater. Chem.*, 2012, **22**, 6603.
23. K. Sharma, Y. H. Kim, J. Gabitto, R. T. Mayes, S. Yiacoumi, H. Z. Bilheux, L. M. Walker, S. Dai and C. Tsouris, Transport of ions in mesoporous carbon electrodes during capacitive deionization of high-salinity solutions, *Langmuir*, 2015, **31**, 1038-1047.
24. X. Xu, H. Tan, Z. Wang, C. Wang, L. Pan, Y. V. Kaneti, T. Yang and Y. Yamauchi, Extraordinary capacitive deionization performance of highly-ordered mesoporous carbon nano-polyhedra for brackish water desalination, *Environ. Sci.: Nano*, 2019, **6**, 981-989.
25. S. Zhao, T. Yan, H. Wang, J. Zhang, L. Shi and D. Zhang, Creating 3D hierarchical carbon architectures with micro-, meso-, and macropores via a simple self-blowing strategy for a flow-through deionization capacitor, *ACS Appl. Mater. Interfaces*, 2016, **8**, 18027-18035.
26. R. T. Mayes, C. Tsouris, J. O. Kiggans Jr, S. M. Mahurin, D. W. DePaoli and S. Dai, Hierarchical ordered mesoporous carbon from phloroglucinol-glyoxal and its application in capacitive deionization of brackish water, *J. Mater. Chem.*, 2010, **20**, 8674.
27. X. Wen, D. Zhang, L. Shi, T. Yan, H. Wang and J. Zhang, Three-dimensional hierarchical porous carbon with a bimodal pore arrangement for capacitive deionization, *J. Mater. Chem.*, 2012, **22**, 23835.
28. H. Wang, D. Zhang, T. Yan, X. Wen, J. Zhang, L. Shi and Q. Zhong, Three-dimensional macroporous graphene architectures as high performance electrodes for capacitive deionization, *J. Mater. Chem. A*, 2013, **1**, 11778.
29. H. Wang, L. Shi, T. Yan, J. Zhang, Q. Zhong and D. Zhang, Design of graphene-coated hollow mesoporous carbon spheres as high performance electrodes for capacitive deionization, *J. Mater. Chem. A*, 2014, **2**, 4739-4750.
30. J. Kim, Y. Yi, D.-H. Peck, S.-H. Yoon, D.-H. Jung and H. S. Park, Controlling hierarchical porous structures of rice husk derived carbons for improved performances of capacitive deionization, *Environ. Sci.: Nano*, 2019, **6**, 916-924.
31. H. K. Furukawa, N.; Go, Y. B.; Aratani, N.; Choi, S. B.; Choi, and A. O. S. E.; Yazaydin, R. Q.; O'Keeffe, M.; Kim, J.; Yaghi, O. M., Ultrahigh porosity in metal-organic frameworks, *Science*, 2010, **329**, 424-428.
32. L. Carlucci, G. Ciani, D. M. Proserpio, T. G. Mitina and V. A. Blatov, Entangled two-dimensional coordination networks: a general survey, *Chem. Rev.*, 2014, **114**, 7557-7580.
33. H. Sung Cho, H. Deng, K. Miyasaka, Z. Dong, M. Cho, A. V. Neimark, J. Ku Kang, O. M. Yaghi and O. Terasaki, Extra adsorption and adsorbate superlattice formation in metal-organic frameworks, *Nature*, 2015, **527**, 503-507.
34. Y. Z. Chen, C. Wang, Z. Y. Wu, Y. Xiong, Q. Xu, S. H. Yu and H. L. Jiang, From bimetallic metal‐organic framework to porous carbon: high surface area and multicomponent active dopants for excellent electrocatalysis, *Adv. Mater.*, 2015, **27**, 5010-5016.
35. B. Y. Guan, L. Yu and X. W. Lou, A dual-metal–organic-framework derived electrocatalyst for oxygen reduction, *Energy Environ. Sci.*, 2016, **9**, 3092-3096.
36. J. Tang, R. R. Salunkhe, J. Liu, N. L. Torad, M. Imura, S. Furukawa and Y. Yamauchi, Thermal conversion of core–shell metal–organic frameworks: a new method for selectively functionalized nanoporous hybrid carbon, *J. Am. Chem. Soc.*, 2015, **137**, 1572-1580.
37. F. Zheng, Y. Yang and Q. Chen, High lithium anodic performance of highly nitrogen-doped porous carbon prepared from a metal-organic framework, *Nat. Commun.*, 2014, **5**. 5261.
38. H. B. Wu, B. Y. Xia, L. Yu, X. Y. Yu and X. W. Lou, Porous molybdenum carbide nano-octahedrons synthesized via confined carburization in metal-organic frameworks for efficient hydrogen production, *Nat. Commun.*, 2015, **6**, 6512.
39. B. Y. Xia, Y. Yan, N. Li, H. B. Wu, X. W. Lou and X. Wang, A metal–organic framework-derived bifunctional oxygen electrocatalyst, *Nat. Energy*, 2016, **1**, 15006.
40. N. L. Torad, Y. Li, S. Ishihara, K. Ariga, Y. Kamachi, H.-Y. Lian, H. Hamoudi, Y. Sakka, W. Chaikittisilp, K. C. W. Wu and Y. Yamauchi, MOF-derived Nanoporous Carbon as Intracellular Drug Delivery Carriers, *Chem. Lett.*, 2014, **43**, 717-719.
41. W. Zhang, X. Jiang, X. Wang, Y. V. Kaneti, Y. Chen, J. Liu, J. S. Jiang, Y. Yamauchi and M. Hu, Spontaneous Weaving of Graphitic Carbon Networks Synthesized by Pyrolysis of ZIF-67 Crystals, *Angew. Chem. Int. Ed. Engl.*, 2017, **56**, 8435-8440.
42. C. Young, R. R. Salunkhe, J. Tang, C. C. Hu, M. Shahabuddin, E. Yanmaz, M. S. Hossain, J. H. Kim and Y. Yamauchi, Zeolitic imidazolate framework (ZIF-8) derived nanoporous carbon: The effect of carbonization temperature on the supercapacitor performance in an aqueous electrolyte, *Phys. Chem. Chem. Phys.*, 2016, **18**, 29308-29315.
43. X. Xu, C. Li, C. Wang, L. Ji, Y. V. Kaneti, H. Huang, T. Yang, K. C. W. Wu and Y. Yamauchi, Three-Dimensional Nanoarchitecture of Carbon Nanotube-Interwoven Metal–Organic Frameworks for Capacitive Deionization of Saline Water, *ACS Sustainable Chem. Eng.*, 2019, **7**, 13949-13954.
44. L. Chang, J. Li, X. Duan and W. Liu, Porous carbon derived from Metal–organic framework (MOF) for capacitive deionization electrode, *Electrochim. Acta*, 2015, **176**, 956-964.

45. Y. Liu, X. Xu, M. Wang, T. Lu, Z. Sun and L. Pan, Metal–organic framework-derived porous carbon polyhedra for highly efficient capacitive deionization, *Chem. Commun.*, 2015, **51**, 12020-12023.
46. Z. Wang, T. Yan, L. Shi and D. Zhang, In Situ Expanding Pores of Dodecahedron-like Carbon Frameworks Derived from MOFs for Enhanced Capacitive Deionization, *ACS Appl. Mater. Interfaces*, 2017, **9**, 15068-15078.
47. Z. Wang, T. Yan, J. Fang, L. Shi and D. Zhang, Nitrogen-doped porous carbon derived from a bimetallic metal–organic framework as highly efficient electrodes for flow-through deionization capacitors, *J. Mater. Chem. A*, 2016, **4**, 10858-10868.
48. J. Zhang, J. Fang, J. Han, T. Yan, L. Shi and D. Zhang, N, P, S co-doped hollow carbon polyhedra derived from MOF-based core–shell nanocomposites for capacitive deionization, *J. Mater. Chem. A*, 2018, **6**, 15245-15252.
49. Z. Wang, T. Yan, G. Chen, L. Shi and D. Zhang, High Salt Removal Capacity of Metal–Organic Gel Derived Porous Carbon for Capacitive Deionization, *ACS Sustainable Chem. Eng.*, 2017, **5**, 11637-11644.
50. T. Gao, H. Li, F. Zhou, M. Gao, S. Liang and M. Luo, *Desalination*, 2019, **451**, 133-138.
51. T. Gao, Y. Du and H. Li, Preparation of nitrogen-doped graphitic porous carbon towards capacitive deionization with high adsorption capacity and rate capability, *Sep. Purif. Technol.*, 2019, **211**, 233-241.
52. J. Han, L. Shi, T. Yan, J. Zhang and D. Zhang, Removal of ions from saline water using N, P co-doped 3D hierarchical carbon architectures via capacitive deionization, *Environ. Sci. Nano*, 2018, **5**, 2337-2345.
53. M. Wang, X. Xu, J. Tang, S. Hou, M. S. A. Hossain, L. Pan and Y. Yamauchi, High performance capacitive deionization electrodes based on ultrathin nitrogen-doped carbon/graphene nano-sandwiches, *Chem. Commun.*, 2017, **53**, 10784-10787.
54. T. Yang, T. Qian, M. Wang, X. Shen, N. Xu, Z. Sun and C. Yan, A sustainable route from biomass byproduct okara to high content nitrogen‐doped carbon sheets for efficient sodium ion batteries, *Adv. Mater.*, 2016, **28**, 539-545.
55. G. Zhao, G. Zou, X. Qiu, S. Li, T. Guo, H. Hou and X. Ji, Rose-like N-doped porous carbon for advanced sodium storage, *Electrochim. Acta*, 2017, **240**, 24-30.
56. D. Li, H. Chen, G. Liu, M. Wei, L.-x. Ding, S. Wang and H. Wang, Porous nitrogen doped carbon sphere as high performance anode of sodium-ion battery, *Carbon*, 2015, **94**, 888-894.
57. S. Yang, L. Peng, P. Huang, X. Wang, Y. Sun, C. Cao and W. Song, *Angew. Chem. Int. Ed.*, 2016, 55, 4016-4020.
58. X. Xu, A. E. Allah, C. Wang, H. Tan, A. A. Farghali, M. H. Khedr, V. Malgras, T. Yang and Y. Yamauchi, Nitrogen, Phosphorus, and Sulfur Co‐Doped Hollow Carbon Shell as Superior Metal‐Free Catalyst for Selective Oxidation of Aromatic Alkanes, *Chem. Eng. J.*, 2019, **362**, 887-896.
59. Y. Huang, J. Yang, L. Hu, D. Xia, Q. Zhang, Y. Liao, H. Li, W. Yang, C. He and D. Shu, Mycelial pellet-derived heteroatom-doped carbon nanosheets with a three-dimensional hierarchical porous structure for efficient capacitive deionization, *Environ. Sci.: Nano,* 2019, **6**, 1430-1442.
60. D. Li, X.-a. Ning, Y. Huang and S. Li, Nitrogen-rich microporous carbon materials for high-performance membrane capacitive deionization, *Electrochim. Acta*, 2019, **312**, 251-262.
61. A. C. Ferrari and J. Robertson, Interpretation of Raman spectra of disordered and amorphous carbon, *Phys.Rev.B*, 2000, **61**, 14095-14107.
62. A. C. Ferrari, J. C. Meyer, V. Scardaci, C. Casiraghi, M. Lazzeri, F. Mauri, S. Piscanec, D. Jiang, K. S. Novoselov, S. Roth and A. K. Geim, Raman Spectrum of Graphene and Graphene Layers, *Phys. Rev. Lett.*, 2006, **97**, 187401.
63. Y. Lv, L. Gan, M. Liu, W. Xiong, Z. Xu, D. Zhu and D. S. Wright, A self-template synthesis of hierarchical porous carbon foams based on banana peel for supercapacitor electrodes, *J. Power Sources*, 2012, **209**, 152-157.
64. A. Ejaz and S. Jeon, The individual role of pyrrolic, pyridinic and graphitic nitrogen in the growth kinetics of Pd NPs on N-rGO followed by a comprehensive study on ORR , *Int. J. Hydrogen Energy*, 2018, **43**, 5690-5702.
65. Y. Zou, W. Zhong, S. Li, J. Luo, C. Xiong and W. Yang, Structure of functionalized nitrogen-doped graphene hydrogels derived from isomers of phenylenediamine and graphene oxide based on their high electrochemical performance, *Electrochim. Acta*, 2016, **212**, 828-838.
66. S. Tian, J. Wu, X. Zhang, K. Ostrikov and Z. Zhang, Capacitive deionization with nitrogen-doped highly ordered mesoporous carbon electrodes, *Chem. Eng. J.*, 2020, **380**, 122514.
67. Z. R. Ismagilov, A. E. Shalagina, O. Y. Podyacheva, A. V. Ischenko, L. S. Kibis, A. I. Boronin, Y. A. Chesalov, D. I. Kochubey, A. I. Romanenko, O. B. Anikeeva, T. I. Buryakov and E. N. Tkachev, Structure and electrical conductivity of nitrogen-doped carbon nanofiber, *Carbon*, 2009, **47**, 1922-1929.
68. W. Zhang, Y. Xia, J. Ju, L. Wang, Z. Fang and M. Zhang, Electrical conductivity of nitride carbon films with different nitrogen content, *Solid State Commun.*, 2003, **126**, 163-166.
69. L. Yang, S. Cheng, Y. Ding, X. Zhu, Z. L. Wang and M. Liu, Hierarchical network architectures of carbon fiber paper supported cobalt oxide nanonet for high-capacity pseudocapacitors, *Nano Lett.*, 2012, **12**, 321-325.
70. Y. Li, Z. Li and P. K. Shen, Simultaneous formation of ultrahigh surface area and three‐dimensional hierarchical porous graphene‐like networks for fast and highly stable supercapacitors, *Adv. Mater.*, 2013, **25**, 2474-2480.
71. L. Miao, H. Duan, M. Liu, W. Lu, D. Zhu, T. Chen, L. Li and L. Gan, Poly (ionic liquid)-derived, N, S-codoped ultramicroporous carbon nanoparticles for supercapacitors, *Chem. Eng. J.*, 2017, **317**, 651-659.
72. Y. Liu, T. Chen, T. Lu, Z. Sun, D. H. C. Chua and L. Pan, Nitrogen-doped porous carbon spheres for highly efficient capacitive deionization, *Electrochim. Acta*, 2015, **158**, 403-409.
73. Y. Liu, X. Xu, M. Wang, T. Lu, Z. Sun and L. Pan, Nitrogen-doped carbon nanorods with excellent capacitive deionization ability, *J. Mater. Chem. A*, 2015, **3**, 17304-17311.
74. M. Ding, F.-H. Du, B. Liu, Z. Y. Leong, L. Guo, F. Chen, A. Baji and H. Y. Yang, Rod-like nitrogen-doped carbon hollow shells for enhanced capacitive deionization, *FlatChem*, 2018, **7**, 10-17.
75. S. Zhao, T. Yan, Z. Wang, J. Zhang, L. Shi and D. Zhang, Removal of NaCl from saltwater solutions using micro/mesoporous carbon sheets derived from watermelon peel via deionization capacitors, *RSC Adv.*, 2017, **7**, 4297-4305.
76. G. Luo, Y. Wang, L. Gao, D. Zhang and T. Lin, Graphene bonded carbon nanofiber aerogels with high capacitive deionization capability, *Electrochim. Acta*, 2018, **260**, 656-663.

77. H. Wang, T. Yan, P. Liu, G. Chen, L. Shi, J. Zhang, Q. Zhong and D. Zhang, In situ creating interconnected pores across 3D graphene architectures and their application as high performance electrodes for flow-through deionization capacitors, *J. Mater. Chem. A*, 2016, **4**, 4908-4919.
78. S. Zhao, T. Yan, H. Wang, G. Chen, L. Huang, J. Zhang, L. Shi and D. Zhang, High capacity and high rate capability of nitrogen-doped porous hollow carbon spheres for capacitive deionization, *Appl. Surf. Sci.*, 2016, **369**, 460-469.
79. J. Shen, Y. Li, C. Wang, R. Luo, J. Li, X. Sun, J. Shen, W. Han and L. Wang, Hollow ZIFs-derived nanoporous carbon for efficient capacitive deionization, *Electrochim. Acta*, 2018, **273**, 34-42.
80. Z. Wang, X. Xu, J. Kim, V. Malgras, R. Mo, C. Li, Y. Lin, H. Tan, J. Tang, L. Pan, Y. Bando, T. Yang and Y. Yamauchi, Nanoarchitectured metal–organic framework/polypyrrole hybrids for brackish water desalination using capacitive deionization, *Mater. Horiz.,* 2019, **6**, 1433-1437.
81. J. W. T. Brezesinski, J. Polleux, B. Dunn and S. H. Tolbert, Templated Nanocrystal-Based Porous TiO2 Films for Next-Generation Electrochemical Capacitors, *J. Am. Chem. Soc.*, 2009, **131**, 1802-1809.
82. T. Kim and J. Yoon, CDI ragone plot as a functional tool to evaluate desalination performance in capacitive deionization, *RSC Adv.*, 2015, **5**, 1456-1461.
83. Y. Wimalasiri, M. Mossad and L. Zou, Thermodynamics and kinetics of adsorption of ammonium ions by graphene laminate electrodes in capacitive deionization, *Desalination*, 2015, **357**, 178-188.
84. P. M. B. R. Zhao, H. Miedema, H. Bruning, and A. van der Wal, Charge efficiency: a functional tool to probe the double-layer structure inside of porous electrodes and application in the modeling of capacitive deionization, *J. Phys. Chem. Lett*, 2010, **1**, 205-210.
85. Y. Liu, L. Pan, X. Xu, T. Lu, Z. Sun and D. H. C. Chua, Enhanced desalination efficiency in modified membrane capacitive deionization by introducing ion-exchange polymers in carbon nanotubes electrodes, *Electrochim. Acta*, 2014, **130**, 619-624.
86. Y. Liu, X. Xu, T. Lu, Z. Sun, D. H. C. Chua and L. Pan, Nitrogen-doped electrospun reduced graphene oxide–carbon nanofiber composite for capacitive deionization, *RSC Adv.*, 2015, **5**, 34117-34124.
87. Y. Liu, T. Lu, Z. Sun, D. H. C. Chua and L. Pan, Ultra-thin carbon nanofiber networks derived from bacterial cellulose for capacitive deionization, *J. Mater. Chem. A*, 2015, **3**, 8693-8700.

